

# Probing the major driver of stellar population properties over sub-galaxy scales with SDSS MaNGA IFU spectroscopy

I. Ferreras<sup>1,2,3\*</sup>, M. Trevisan<sup>4</sup>, O. Lahav<sup>1</sup>, R. R. de Carvalho<sup>5</sup>, J. Silk<sup>6,7,8</sup>

<sup>1</sup> *Department of Physics and Astronomy, University College London, London WC1E 6BT, UK*

<sup>2</sup> *Instituto de Astrofísica de Canarias, Calle Vía Láctea s/n, E38205, La Laguna, Tenerife, Spain*

<sup>3</sup> *Departamento de Astrofísica, Universidad de La Laguna, E38206 La Laguna, Tenerife, Spain*

<sup>4</sup> *Departamento de Astronomia, Universidade Federal do Rio Grande do Sul, 91501-970 Porto Alegre-RS, Brazil*

<sup>5</sup> *NAT - Universidade Cidade de São Paulo, 01506-000, SP, Brazil*

<sup>6</sup> *Institut d'Astrophysique de Paris, 98 bis Boulevard Arago, F-75014 Paris, France*

<sup>7</sup> *BIPAC, Department of Physics, University of Oxford, Keble Road, Oxford OX1 3RH, UK*

<sup>8</sup> *Department of Physics and Astronomy, The Johns Hopkins University, Baltimore, MD 21218, USA*

Submitted for publication in MNRAS, December 4th, 2024

## ABSTRACT

Thanks to Integral Field Unit survey data it is possible to explore in detail the link between the formation of the stellar content in galaxies and the drivers of evolution. Traditionally, scaling relations have connected galaxy-wide parameters such as stellar mass ( $M_s$ ), morphology or average velocity dispersion ( $\sigma$ ) to the star formation histories (SFHs). We study a high quality sample of SDSS-MaNGA spectra to test the possibility that sub-galaxy ( $\sim 2$  kpc) scales are dominant, instead of galaxy-wide parameters. We find a strong correlation between *local* velocity dispersion and key line strengths that depend on the SFHs, allowing us to make the ansatz that this indicator – that maps the local gravitational potential – is the major driver of star formation in galaxies, whereas larger scales play a role of a secondary nature. Galactocentric distance has a weaker correlation, suggesting that the observed radial gradients effectively reflect local variations of velocity dispersion. In our quest for a cause, instead of a correlation, we contrast  $\sigma$  with local stellar mass, that appears less correlated with population properties. We conclude that the inherently higher uncertainty in  $M_s$  may explain its lower correlation with respect to  $\sigma$ , but the extra uncertainty needed for  $\sigma$  to have similar correlations as  $M_s$  is rather high. Therefore we posit local velocity dispersion as the major driver of evolution, a result that should be reproduced by hydrodynamical models at the proper resolution.

**Key words:** galaxies: evolution – galaxies: stellar content – galaxies: statistics – galaxies: fundamental parameters – techniques: spectroscopic – methods: data analysis

## 1 INTRODUCTION

Over the past two decades, large scale spectroscopic surveys have revolutionised our understanding of extragalactic astrophysics. Before these large datasets became available, most studies were based on relatively small numbers of well-chosen targets. Survey data enable us to tackle this problem in a statistical sense, looking for the general trends that reveal the fundamental processes driving the formation of galaxies, confronting the observations with models that encapsulate the main mechanisms transforming gas into stars and framing this in a cosmological context. Scaling trends such as the colour-magnitude relation, the fundamental plane, or the Tully-Fisher relation provide evidence of a strong trend between a local physical quantity, say gravitational potential in its many guises, and the formation of galaxies. For instance, we now know that there is a strong correlation between the

age and the mass of a galaxy, with more massive systems being preferentially older, and predominantly supported as hot dynamical systems (see, e.g., [Silk & Mamon 2012](#), for a general review). The well-established bimodality (e.g., [Strateva et al. 2001a](#); [Baldry et al. 2004](#); [Anghopo et al. 2019](#)) reveals a blue cloud/red sequence transition where the processes that quench star formation appear to hold the key to understanding how galaxies evolve. In this context, an important issue concerns the “drivers” of galaxy formation, i.e. the fundamental properties that control this evolution. A large number of papers look for these drivers, mainly proposing options at the galactic level, i.e. scales of several kpc, vs environment, group/cluster scales of hundreds of kpc and beyond (to name a few, [Weinmann et al. 2006](#); [Peng et al. 2010](#); [Rogers et al. 2010](#); [Etherington & Thomas 2015](#)). At the galaxy level, relevant parameters are the mass, velocity dispersion, gravitational potential, dynamical support or morphology. The more recent IFU-based surveys (e.g. [Bacon et al. 2001](#); [Cappellari et al. 2011a](#); [Sánchez et al. 2012](#); [Bryant et al. 2015](#); [Bundy](#)

\* E-mail: i.ferreras@ucl.ac.uk

et al. 2015a) brought this analysis into a new level, as galaxies could be probed spectroscopically in much more detail, regarding both the dynamical state and the stellar population content, with fundamental results into the way these two aspects relate to each other (e.g., Cappellari et al. 2011b; Wang et al. 2024).

While many of the IFU-based studies statistically approach the spatially resolved properties with radial gradients of targeted observables, such a result only produces a first view of resolved galaxy formation, and depends on how the local properties match with galactocentric distance. Gradient studies of stellar populations reveal interesting trends where the central regions tend to be dominated by old, metal rich stars, whereas the outer regions tend to be metal poorer, reflecting a different formation mode (see, e.g. Kuntschner et al. 2010; La Barbera et al. 2012; González Delgado et al. 2015; Greene et al. 2015; Parikh et al. 2018, 2021; Ferreras et al. 2019; Zibetti et al. 2020). These observational trends can be explained within a simple framework based on simulations (Oser et al. 2010), where most of the formation of a galaxy is separated into two major phases, an in-situ phase that generates the stellar component of the most massive, parent, halo, and the ex-situ phase that consists of later additions to the galaxy from mergers (Naab et al. 2009). While this working hypothesis is a powerful way to understand the spatially resolved results, it hardwires the interpretation to monolithic versus hierarchical growth.

In a insightful review, Sánchez et al. (2021) suggested that local properties within galaxies are also subject to the same scaling relations as those found over galaxy scales, so that the latter can be interpreted as an integrated version of the former. Such an interpretation goes back to scaling relations such as the Schmidt-Kennicutt law that defines the star formation rate by the local gas density, either as a projected surface density (Kennicutt 1989) or the 3D volume density (Schmidt 1959). Local relations provide a more detailed framework than the standard two-phase scenario and give small scale mechanisms a more important role. Our paper takes this point further, adopting the ansatz that a local observable – roughly defined over a physical scale of  $\sim 2$  kiloparsec (limited by the size of the optical fibre) – mostly controls the overall properties of the stellar populations, therefore also determining its past star formation and chemical enrichment histories. The excellent quality of the publicly available data from the SDSS-IV IFU survey MaNGA (Bundy et al. 2015b) allows us to tackle such a proposal. In addition, we also explore which of the typical local properties are more strongly correlated, and thus can potentially serve as the major driver of galaxy evolution. Our conclusions strongly favour *local* stellar velocity dispersion as the dominant driver. Such a hypothesis requires a revision of some of the established ideas regarding galaxy formation, and offers a strong constrain to test the validity of hydrodynamical cosmological simulations.

This paper is structured as follows. After this introductory section, we describe the MaNGA IFU dataset in Section 2, followed by the description of the scaling properties in Section 3 that motivate us to propose the ansatz that the star formation histories are mainly controlled by physical quantities over sub-galaxy scales, with the velocity dispersion ( $\sigma$ ) posited as the main driver. Thus far these trends are shown as observational correlations. In Section 4 we further consider

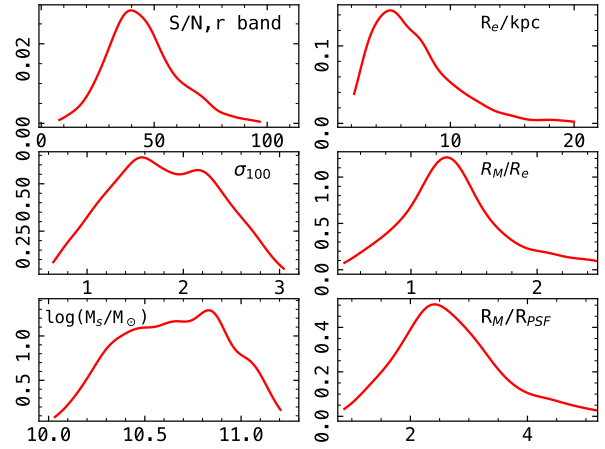


**Figure 1.** Distribution of general observables of the galaxy sample from SDSS-MaNGA. The corresponding parameter (horizontal axis) is labelled in each panel. Clockwise from top-left we show the signal to noise ratio of the spectra within one effective radius in the SDSS-*r* band, the effective radius in physical units, the ratio between the galactocentric distance of the outermost useable spaxel in each galaxy ( $R_M$ ) and the effective radius, the ratio between  $R_M$  and  $R_{PSF}$  (i.e. the HWHM of the point spread function), the (logarithm) of the stellar mass in solar units, and the averaged stellar velocity dispersion in units of  $100 \text{ km s}^{-1}$ .

whether  $\sigma$  and not stellar mass represents the cause of these trends. Section 5 takes a look at the connection between the observed local trends and the evolutionary stage of the galaxies. Finally, we summarise our conclusions in Section 6.

## 2 THE SAMPLE

The parent catalogue for this work is the Anghopo et al. (2019, 2020) sample that is based on a detailed analysis of high quality data from the Legacy SDSS spectra, classified into the three standard evolutionary states (blue cloud, green valley and red sequence) using one of the most robust indicators of the stellar population content, the  $4000\text{\AA}$  break strength. That sample is restricted in redshift ( $0.05 \leq z \leq 0.1$ ) and in the signal to noise ratio of the single fibre spectra (median  $S/N > 10$  over pixels in the SDSS-*r* band), and consists of over 200 thousand galaxies. We cross-match this catalogue with the DR17 version (Abdurro’uf et al. 2022) of the SDSS-IV/MaNGA (Bundy et al. 2015b) IFU survey, that comprises  $\sim 10,000$  galaxies. We also make use of the Marvin (Cherinka et al. 2019) data products. The cross-match results in a set of 2,034 galaxies, but one galaxy does not have the science-ready data from Marvin (mangaID 1-80510), and a few other galaxies have repeated observations (see Table 1 from Westfall et al. 2019), for which we retrieve the ones with the best seeing according to the SEEMED keyword. The final set comprises 2,024 galaxies, and constitutes our working sample. Fig. 1 shows the distribution of the sample with respect to a number of important parameters defined in each galaxy observation (clock-wise from top-left: signal-to-noise ratio measured within one effective radius, the physical effective radius in kpc – assuming a vanilla flavoured  $\Lambda$ CDM cosmology with  $h=0.7$  and  $\Omega_m=0.3$  – the galactocentric distance of the outermost useable spaxel ( $R_M$ ) in units of  $R_e$ ,

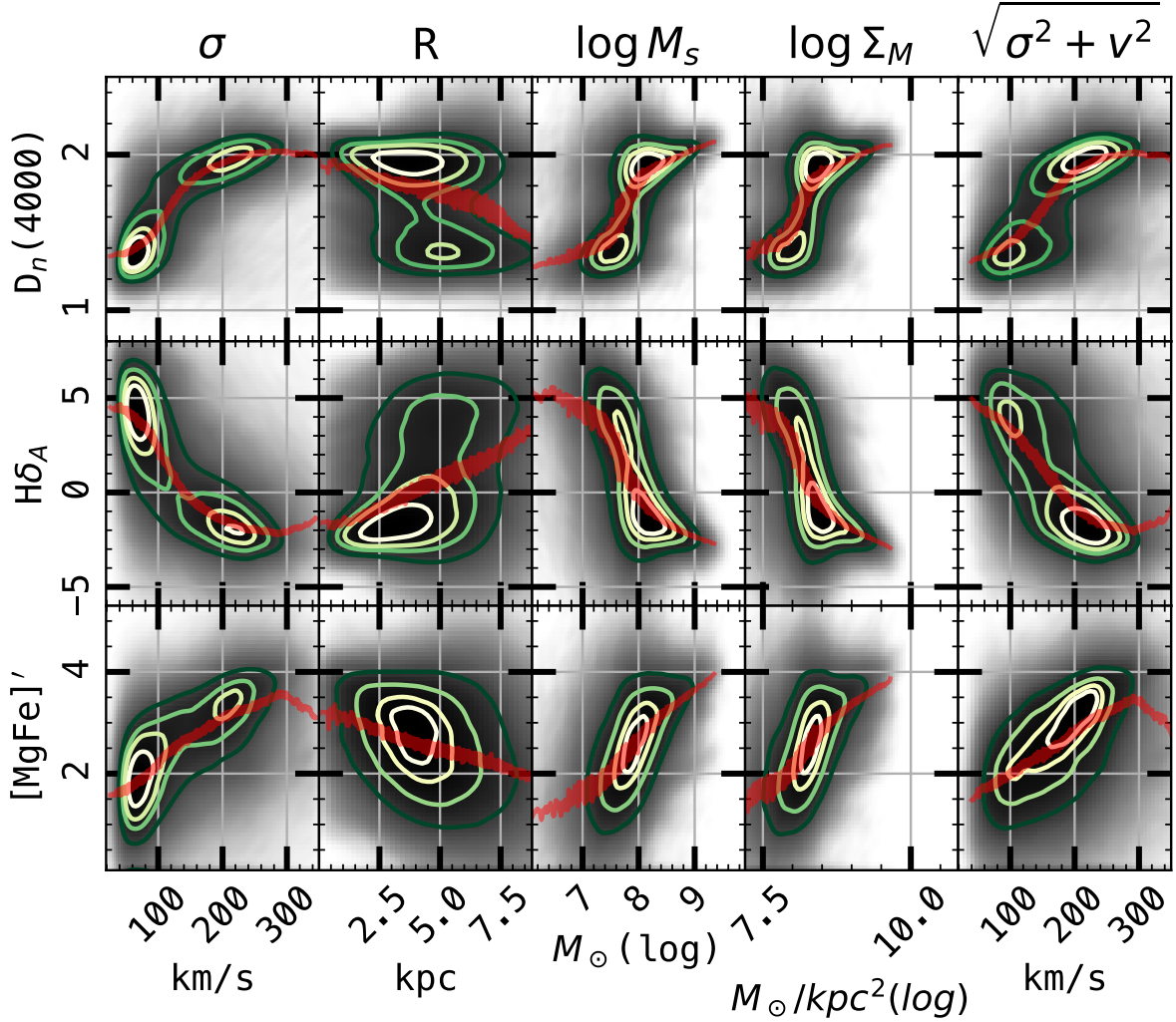


**Figure 2.** Bivariate plots of three fundamental line strengths shown with respect to five indicators of galaxy “position”, as defined for *each individual spaxel*, (from left to right) velocity dispersion, galactocentric distance, stellar mass, surface stellar mass density, and a proxy of kinetic energy,  $\sqrt{\sigma^2 + v^2}$ . The data consists of over 1 million measurements comprising *individual spaxels*, regardless of the galaxies they correspond to. The contours engulf (from the inside out) 25, 50, 75 and 90% of all data points, starting in the regions of higher data point density. The red line in each panel follows the running median of the distribution with respect to the abscissa.

the same  $R_M$  in units of the HWHM of the PSF (defined as  $R_{\text{PSF}}$ ), stellar mass, and velocity dispersion in units of  $100 \text{ km s}^{-1}$ . By “useable” spaxels, we enforce a minimum S/N (also in the SDSS-*r* band) of 5 for *individual spectra*. In addition, we discard spaxels where the individual velocity dispersion estimate is uncertain, or outside of the  $[50, 300] \text{ km/s}$  interval. Both constraints ensure that the resulting individual measurements are reliable. The final sample of 2,024 galaxies produces a set of 1,025,841 spaxels.

The novel approach of this paper lies in our relinquishing the connection of the data with the “host” galaxy, turning instead to the analysis of *individual spaxels*, representing local regions of galaxy formation and evolution. In other words, we consider this sample as a set of over one million good quality independent spectra of local star forming regions. At the median redshift of the sample ( $z_M=0.065$ ), the size of a spaxel fibre (2arcsec diameter) maps a physical scale of 2.5kpc. We explore several types of “local indicators”: stellar

velocity dispersion ( $\sigma$ , measured locally in each spaxel), projected galactocentric distance ( $R$ ), stellar mass ( $M_s$ ), stellar mass surface density ( $\Sigma_M$ , defined as the ratio between the stellar mass in the spaxel and the physical area spanned by the fibre at the location of the galaxy) and the bulk velocity ( $v$ ). These indicators can be defined in an absolute sense (i.e. each spaxel is labelled by a  $\sigma$  in  $\text{km/s}$ , an  $R$  in kpc, a  $M_s$  in  $M_\odot$ , a  $\Sigma_M$  in  $M_\odot \text{ kpc}^{-2}$ ), or as a relative dimensionless quantity:  $\sigma$ ,  $M_s$  and  $\Sigma_M$  being given as a fraction of the maximum value of the relevant quantity in the corresponding galaxy, and  $R$  measured in units of the effective radius,  $R_e$ . For the bulk velocity, we use two definitions: the absolute measurement combines it with velocity dispersion,  $\sqrt{\sigma^2 + v^2}$  and serves as a proxy of kinetic energy. The relative definition is the standard ratio  $|v|/\sigma$  that traces the level of rotational support versus random motion, a direct indicator of morphology (see, e.g., Cappellari et al. 2011b). In Appendix A, we show the distribution of spaxel measurements for a few

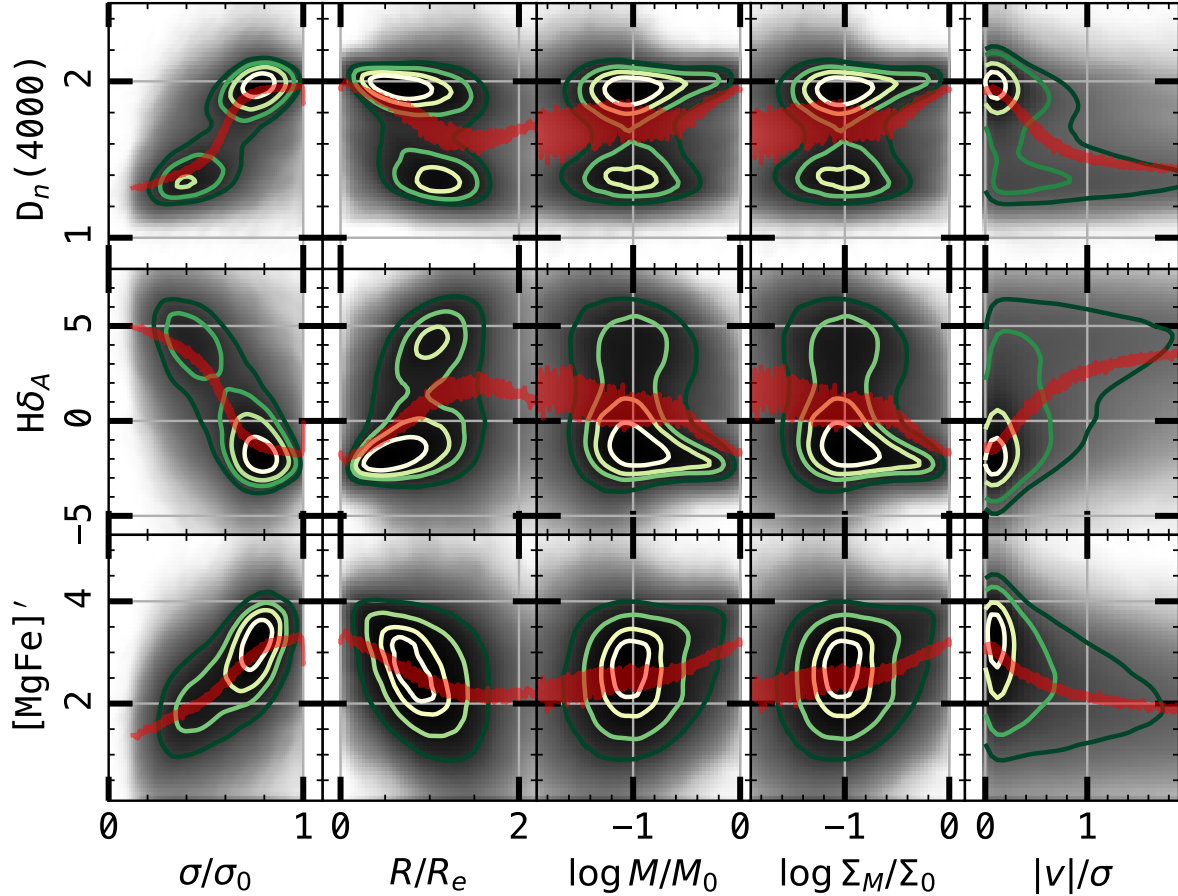


**Figure 3.** Equivalent of Fig. 2 for relative observables, as described in the text. In addition to (from left to right) stellar velocity dispersion, galactocentric distance, stellar mass and stellar mass surface density, we also include the ratio between the absolute value of bulk velocity and velocity dispersion of the stellar component, as an estimator of rotational support. All measures are referred to over 1 million individual spaxels. The contours engulf (from the inside out) 25, 50, 75 and 90% of all data points, starting in the regions of higher data point density. The red line in each panel tracks the running median of the distribution with respect to the abscissa.

individual galaxies, comparing them with respect to the distribution of the complete spaxel sample as we will show in the next section. We emphasize that our analysis rests on the assumption that the statistical distribution of individual spaxels reflects an inherent causality at sub-galaxy ( $\sim 2$  kpc) scales, regardless of the stellar mass, morphology, etc, corresponding to the parent galaxy.

### 3 THE ANSATZ: LOCAL PROPERTIES DRIVE THE AVERAGE STAR FORMATION HISTORY

Fig. 2 shows, as a density plot, the distribution of spaxel data of the whole sample for three targeted line strengths, from top to bottom, the 4000Å break strength, adopting the definition of Balogh et al. (1999), the wide (A) definition of the H $\delta$  Balmer line of Worthey & Ottaviani (1997), and the [MgFe]’ index that combines the traditional Lick indices Mgb, Fe5270 and Fe5335 in a way that minimises the dependence on the [Mg/Fe] abundance ratio (Thomas et al. 2003). These three indices lock a large amount of “information” (in the entropy sense) or variance, so they are ideal indicators to explore the population properties, especially in data cov-

ering a wide range of S/N values (see Ferreras et al. 2023). Very roughly, we can assume that  $D_n(4000)$  traces overall stellar age,  $H\delta_A$  is prominent in regions with recent star formation activity, and [MgFe]’ features a strong dependence with metallicity. However, the reader should be cautious in the interpretation as these indices (or any other) have a substantial age-metallicity degeneracy (e.g. Ferreras et al. 1999; La Barbera et al. 2013), and are strongly correlated with respect to the fundamental population properties (Ferreras et al. 2023). For reference, we also include below the analysis for the stellar age and metallicity derived by adopting a standard methodology (Wilkinson et al. 2017).

Fig. 2 presents the data with respect to the indicators defined in an absolute sense: stellar velocity dispersion ( $\sigma$ , in km/s), galactocentric distance ( $R$ , in kpc), stellar mass ( $M_s$ , in  $M_\odot$ ), stellar mass surface density ( $\Sigma_M$  in  $M_\odot \text{ kpc}^{-2}$ ), and a proxy for the kinetic energy, i.e. combining velocity dispersion and bulk motion in quadrature ( $\sqrt{\sigma^2 + v^2}$  in km/s). We emphasize that these are local indicators, defined for specific spaxels, and all the spaxels in all galaxies from the sample are included here to produce these distributions. In addition to the greyscale density plot, to guide the eye, we overlay con-

**Table 1.** Correlation coefficients between stellar population line strengths and observables measured in an absolute way in spaxels with  $S/N \geq 5$  (see fig 2)

Index	$\sigma$	$R$	$\log M_s$	$\log \Sigma_M$	$\sqrt{\sigma^2 + v^2}$
Correlation coefficient					
$D_n(4000)$	$+0.756 \pm 0.001$	$-0.236 \pm 0.001$	$+0.578 \pm 0.001$	$+0.548 \pm 0.001$	$+0.610 \pm 0.001$
$H\delta_A$	$-0.669 \pm 0.001$	$+0.297 \pm 0.001$	$-0.562 \pm 0.001$	$-0.563 \pm 0.001$	$-0.522 \pm 0.001$
$[MgFe]'$	$+0.548 \pm 0.001$	$-0.310 \pm 0.001$	$+0.518 \pm 0.001$	$+0.511 \pm 0.001$	$+0.401 \pm 0.001$
$\log t_{LW}$	$+0.361 \pm 0.001$	$-0.162 \pm 0.001$	$+0.614 \pm 0.001$	$+0.645 \pm 0.001$	$+0.275 \pm 0.001$
$\log t_{MW}$	$+0.183 \pm 0.001$	$-0.045 \pm 0.001$	$+0.434 \pm 0.001$	$+0.466 \pm 0.001$	$+0.134 \pm 0.001$
$\log Z_{LW}$	$+0.490 \pm 0.001$	$-0.198 \pm 0.001$	$+0.476 \pm 0.001$	$+0.454 \pm 0.001$	$+0.452 \pm 0.001$
$\log Z_{MW}$	$+0.403 \pm 0.001$	$-0.144 \pm 0.001$	$+0.454 \pm 0.001$	$+0.433 \pm 0.001$	$+0.350 \pm 0.001$
Standard deviation (and $1\sigma$ error)					
$D_n(4000)$	$0.169 \pm 0.037$	$0.273 \pm 0.019$	$0.223 \pm 0.050$	$0.228 \pm 0.050$	$0.213 \pm 0.027$
$H\delta_A$	$2.139 \pm 0.328$	$2.888 \pm 0.289$	$2.428 \pm 0.577$	$2.413 \pm 0.597$	$2.516 \pm 0.244$
$[MgFe]'$	$0.818 \pm 0.042$	$0.930 \pm 0.122$	$0.828 \pm 0.124$	$0.830 \pm 0.139$	$0.881 \pm 0.047$
$\log t_{LW}$	$0.234 \pm 0.025$	$0.252 \pm 0.038$	$0.188 \pm 0.037$	$0.179 \pm 0.033$	$0.243 \pm 0.016$
$\log t_{MW}$	$0.216 \pm 0.030$	$0.221 \pm 0.030$	$0.188 \pm 0.041$	$0.182 \pm 0.039$	$0.219 \pm 0.021$
$\log Z_{LW}$	$0.142 \pm 0.026$	$0.165 \pm 0.016$	$0.142 \pm 0.034$	$0.145 \pm 0.033$	$0.147 \pm 0.020$
$\log Z_{MW}$	$0.235 \pm 0.070$	$0.266 \pm 0.039$	$0.224 \pm 0.074$	$0.226 \pm 0.071$	$0.242 \pm 0.058$

**Table 2.** Correlation coefficients between stellar population line strengths and observables measured in a relative way in spaxels with  $S/N \geq 5$  (see fig 3)

Index	$\sigma/\sigma_0$	$R/R_e$	$\log M_s/M_0$	$\log \Sigma_M/\Sigma_0$	$ v /\sigma$
Correlation coefficient					
$D_n(4000)$	$+0.651 \pm 0.001$	$-0.207 \pm 0.001$	$+0.062 \pm 0.001$	$+0.060 \pm 0.001$	$+0.036 \pm 0.001$
$H\delta_A$	$-0.605 \pm 0.001$	$+0.240 \pm 0.001$	$-0.117 \pm 0.001$	$-0.117 \pm 0.001$	$-0.007 \pm 0.001$
$[MgFe]'$	$+0.520 \pm 0.001$	$-0.292 \pm 0.001$	$+0.175 \pm 0.001$	$+0.177 \pm 0.001$	$-0.027 \pm 0.002$
$\log t_{LW}$	$+0.317 \pm 0.001$	$-0.111 \pm 0.001$	$+0.398 \pm 0.001$	$+0.396 \pm 0.001$	$-0.004 \pm 0.002$
$\log t_{MW}$	$+0.136 \pm 0.001$	$+0.004 \pm 0.001$	$+0.318 \pm 0.001$	$+0.315 \pm 0.001$	$+0.007 \pm 0.002$
$\log Z_{LW}$	$+0.458 \pm 0.001$	$-0.207 \pm 0.001$	$+0.118 \pm 0.001$	$+0.120 \pm 0.001$	$+0.013 \pm 0.001$
$\log Z_{MW}$	$+0.385 \pm 0.001$	$-0.139 \pm 0.001$	$+0.125 \pm 0.001$	$+0.124 \pm 0.001$	$+0.013 \pm 0.002$
Standard deviation (and $1\sigma$ error)					
$D_n(4000)$	$0.208 \pm 0.030$	$0.274 \pm 0.021$	$0.280 \pm 0.015$	$0.280 \pm 0.015$	$0.234 \pm 0.029$
$H\delta_A$	$2.370 \pm 0.285$	$2.912 \pm 0.347$	$3.001 \pm 0.266$	$3.001 \pm 0.266$	$2.614 \pm 0.257$
$[MgFe]'$	$0.839 \pm 0.035$	$0.933 \pm 0.115$	$0.963 \pm 0.106$	$0.963 \pm 0.106$	$0.889 \pm 0.047$
$\log t_{LW}$	$0.240 \pm 0.026$	$0.254 \pm 0.038$	$0.221 \pm 0.036$	$0.221 \pm 0.036$	$0.244 \pm 0.020$
$\log t_{MW}$	$0.218 \pm 0.028$	$0.222 \pm 0.026$	$0.199 \pm 0.032$	$0.199 \pm 0.032$	$0.218 \pm 0.025$
$\log Z_{LW}$	$0.147 \pm 0.023$	$0.163 \pm 0.021$	$0.167 \pm 0.015$	$0.167 \pm 0.015$	$0.159 \pm 0.016$
$\log Z_{MW}$	$0.241 \pm 0.065$	$0.265 \pm 0.048$	$0.268 \pm 0.031$	$0.268 \pm 0.031$	$0.258 \pm 0.046$

tours at levels that engulf (from the inside out) 25, 50, 75 and 90% of the total set. Each of the indices is corrected for velocity dispersion effects using the term provided in the Marvin dataset (for instance: `specindex_corr_hdeltaa` for the correction of the  $H\delta_A$  line strength, defined as a multiplicative correction). Our hypothesis – that the stellar population content is “driven” by local quantities – is supported by the trends shown in the figure, where the line strengths are strongly correlated with *local* velocity dispersion, regardless of galaxy type, mass, etc. In addition, Fig. 3 shows the same observables defined in the previous figure, but in a relative sense: for  $\sigma$ ,  $M_s$  and  $\Sigma_M$  we take the ratio between the measured value in each spaxel and the maximum of the distribution for each individual galaxy, and for  $R$  it is given as the ratio with respect to the effective radius, taken from the official SDSS/MaNGA data. Finally, we include the ratio between

the bulk velocity in absolute value and the velocity dispersion (both concerning the stellar component).

A first test to determine which of these local indicators is dominant, we calculate the Pearson correlation coefficient ( $r_{XY}$ ) for all the bivariate plots presented in Fig. 2 for absolute observables and Fig. 3 for relative observables. The results are shown in the top portions of Tabs. 1 and 2, respectively. The quoted uncertainties correspond to  $1\sigma$  of the distribution of correlation coefficients derived from 1,000 randomly selected samples each one comprising 75% of the whole set. This coefficient is defined to look for linear trends in data sets. Figs. 2 and 3 show that these correlations are not necessarily linear, but  $r_{XY}$  provides a useful quantification of correlatedness – much in the same way as covariance in non-Gaussian distributions. We also explored non-linear statistics, such as the Spearman correlation coefficient

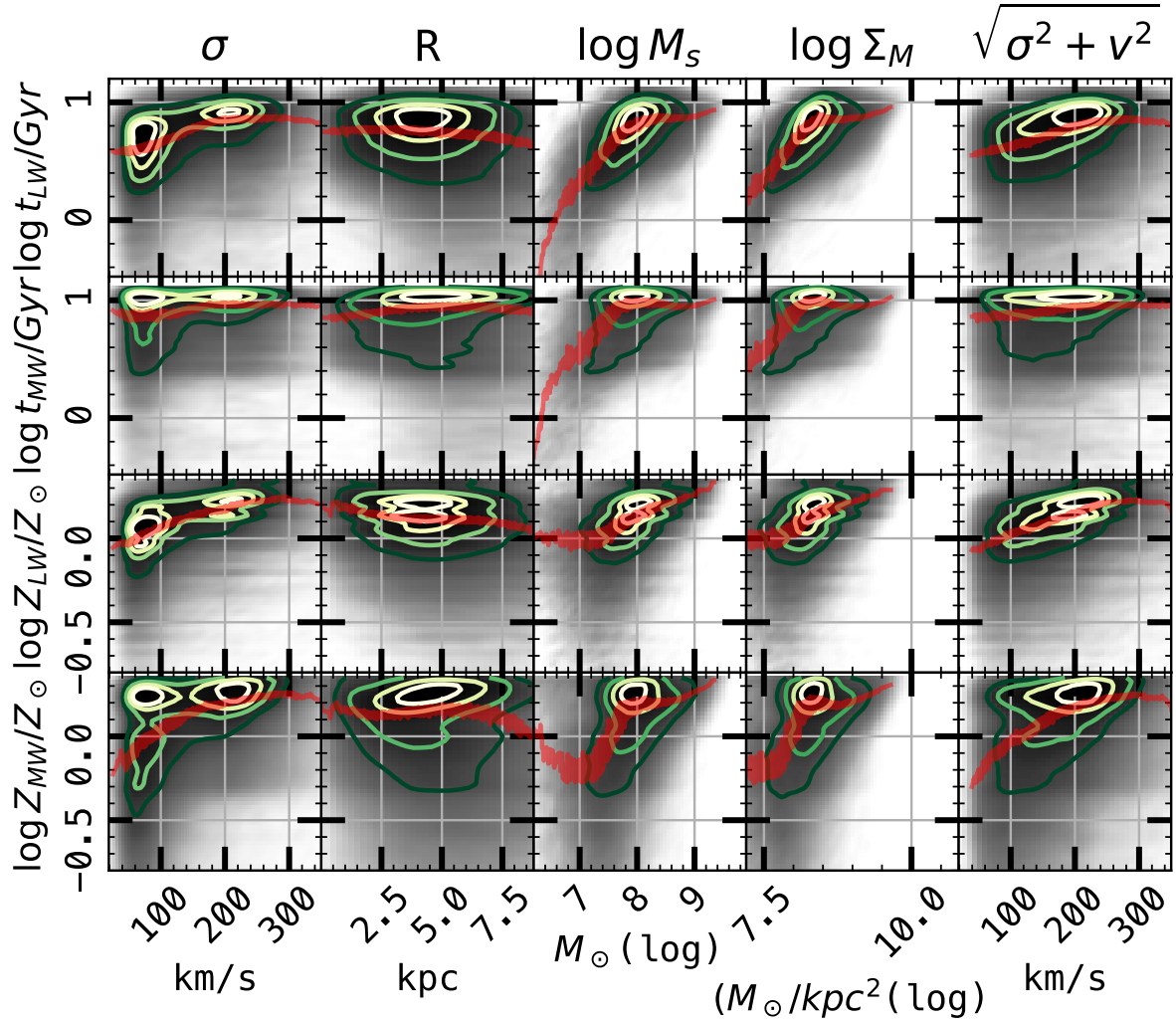


**Figure 4.** Equivalent of Fig. 2 for the Luminosity- (LW) and Mass-Weighted (MW) stellar age and metallicity, as derived from the FireFly fitting procedure (Wilkinson et al. 2017).

( $r_S$ ), which is better suited to track monotonicity. We find very similar results that confirms these results. For instance, the correlation between (absolute) velocity dispersion and  $D_n(4000)$  is  $r_{XY}=+0.756$ ,  $r_S=0.774$ , and the equivalent result for the trend with (absolute) galactocentric radial distance and  $D_n(4000)$  is  $r_{XY}=-0.236$ ,  $r_S=-0.224$ .

A second measure of the correlation, better suited to non-linear trends, say between  $X=\sigma$  and  $Y=D_n(4000)$ , involves producing a running median  $Y_R = f(X)$  by taking sliding intervals (of size 1,000) in increasing  $X$ . For each interval we define the general trend by the running median:  $f(X_i) = \text{median}(X_i)$ , shown as red lines in each panel of Figs. 2 and 3). We now define the residuals with respect to this trend:  $\delta_i \equiv (Y_i - f(X_i))$  for each data point (i.e. spaxel), from which we quote the standard deviation:  $\sqrt{\langle \delta^2 \rangle - \langle \delta \rangle^2}$ , in the bottom portion of Tabs. 1 and 2, along with its own standard deviation, serving as an indicator of the quality of this number as a tracer of correlation.

The strongest correlation is found for stellar (local) velocity dispersion in all three line strengths, especially  $D_n(4000)$ . Note that of the three choices, the  $4000\text{\AA}$  break strength is

the one least sensitive to systematic effects of velocity dispersion<sup>1</sup>, confirming the strong relation between stellar population content and  $\sigma$ , i.e. excluding a potential systematic. Both the absolute case ( $\sigma$  presented in km/s) or the relative one (adopting the dimensionless ratio  $\sigma/\sigma_0$ ) produce similar coefficients, although the latter appears less correlated with population properties. The kinetic energy proxy ( $\sqrt{\sigma^2 + v^2}$ ) is also strongly correlated, but less so than velocity dispersion. Moreover, note the very weak correlation of  $|v|/\sigma$ , which leads us to conclude that the strong correlation found in  $\sqrt{\sigma^2 + v^2}$  is dominated by  $\sigma$ . It is also worth noting that the measured bulk velocity depends on inclination, weakening the expected trends. Regarding stellar mass and stellar mass surface density, it is quite remarkable to note the strong correlation for the absolute estimators (Tab. 1) but the substantially lower level of correlation for the relative observables (Tab. 2). We emphasize that the relative values are simply referenced with respect to the maximum value of the observ-

<sup>1</sup> because it is defined in a wider spectral range.

able in each galaxy. Such a behaviour is not found for velocity dispersion where both absolute and relative estimates appear strongly correlated with the line strengths.

In stark contrast, galactocentric distance is very weakly correlated with any of the population parameters, either in absolute or relative estimates. Our measurements of galactocentric distance adopt the official MaNGA parameter based on the elliptical Petrosian half-light radius as  $R_e$ , a more robust indicator than parameters based on Sérsic fitting (Wake et al. 2017). Note also the jagged behaviour of the running median lines, especially concerning radial distance, produced because of two factors: weaker correlation and in some cases, the presence of a bimodality of line strength measurements within the same range of galactocentric distance. In contrast, the plots with velocity dispersion separate better the two distributions (e.g. strong vs weak 4000Å break strength). We note that while spatial resolution may introduce a systematic, mainly as the size of the PSF is not small with respect to the extent of the observations (see Fig. 1), the effect would induce lower correlations in both galacto-centric distance and velocity dispersion, whereas we find a notable difference between these two local indicators.

In addition to the line strengths directly measured in the spaxels, we include in Fig. 4 the distribution of population parameters derived from the spectra. From bottom to top we show the stellar age (luminosity weighted and mass weighted) and the metallicity (also luminosity weighted and mass weighted). The results are retrieved from the Portsmouth port of the MaNGA database using the Firefly code (Wilkinson et al. 2017). These parameters are now subject to the systematics produced by fitting the spectra to a set of population synthesis models. The same measurements of the correlation coefficient and scatter with respect to the running median is shown for these parameters in Tabs. 1 for absolute indicators and 2 for relative indicators. We should emphasize that the stellar mass used in this work is also dependent on the same type of analysis – in order to translate the observed flux into a stellar mass. Therefore, it comes as no surprise that these parameters show substantial correlation. However stellar velocity dispersion – a more independent observable to the derivation of population parameters – is also found to correlate at a similar level.

#### 4 WHICH ONE IS THE MAJOR DRIVER OF POPULATION PROPERTIES?

Finding the fundamental driver of star formation in galaxies is a complicated task. Most of the work in statistics is geared towards the search, quantification and analysis of correlations, but the mantra of causal inference states that “correlation does not imply causation”<sup>2</sup>. Indeed, interesting cases abound where highly correlated variables clearly do not cause the trend under study – such as the textbook example of the correlation between ice cream sales and drowning, where the fundamental “driver” of the relation is climate (typically called confounder variable, see, e.g. Pearl & Mackenzie 2018). An illustrative point regarding the relationship of the local indicators explored in this paper is shown in Fig. 5, where

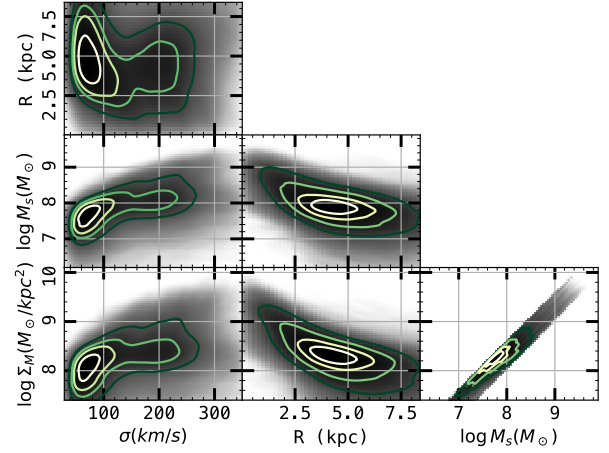


**Figure 5.** Relationship between local indicators, shown as a density plot of the distribution of all spaxel data. The contours engulf (from the inside out) 25, 50, 75 and 90% of all data points, starting from the regions of higher data point density.

the four choices are compared against one another as a density plot. The most conspicuous relation is unsurprisingly found between stellar mass and surface stellar mass density, as both use  $M_s$  and  $\Sigma_M$  simply adds a second variable,  $R$ , that also correlates with stellar mass. A very relevant plot is the weak correlation between  $\sigma$  and  $R$ , that, linked to the previously found correlation with line strengths, leads us to discard galactocentric distance as a key variable in the analysis. Stellar mass and  $\sigma$  do have a substantial correlation, and it is worth noting that these two variables are derived in independent ways, so this trend shows a physical connection. We therefore consider  $\sigma$  and  $M_s$  as candidates of the “main” variable. But which of these two is more important?

A first test is shown in Fig. 6, where the sample is split primarily with respect to velocity dispersion (left column), or stellar mass (right column). In each case, we bin the main variable in ten intervals within which we assume the main variable is roughly “fixed”, i.e. defined by the chosen bin. In each interval, the other variable ( $\log M_s$  when binning in  $\sigma$  and vice-versa) is used to select a subset at the 25th and 75th percentile levels from the distribution. The top panels in each case trivially show the sample selection, with the high (low) subsets shown in red (blue), and the total sample in grey. The points represent the median in each case, along with the standard deviation, shown as an error bar. The middle and bottom panels show the equivalent median and standard deviation of the 4000Å break and the  $H\delta_A$  line strength. The variation in the line strengths at fixed  $\sigma$  is smaller than the corresponding one at fixed stellar mass, suggesting that stellar mass plays some role, but in a subdominant way with respect to velocity dispersion.

Previous studies aiming at the cause of the observed population trends within galaxies only conclude that stellar velocity dispersion is the most correlated variable with stellar populations (see, e.g., Ferreras et al. 2019). However, one could argue that  $\sigma$  is the measurement with the lowest intrinsic uncertainty – its derivation simply depends on a comparison of many absorption lines in the spectrum of the galaxy with a smoothing kernel, and thus minimises the potential systematics regarding the method. In contrast, stellar mass suffers

<sup>2</sup> but sometimes it does!

from a more elaborate set of systematic effects that depend on the modelling of the stellar populations to infer a mass-to-light ratio. We reject radial distance as a major driver, as it suffers from relatively low measurement systematics, and the correlation coefficients are substantially lower than the other local measures (while correlation is not causation, we need a strong correlation to justify the cause). Fig. 7 compares the Pearson correlation coefficient and associated scatter of the running median (as presented in Tab. 1) of the trends between  $D_n(4000)$  (top) or  $H\delta_A$  (bottom) and stellar velocity dispersion. The horizontal axis corresponds to a parameter,  $\Delta$  that represents the standard deviation of an extra component of random Gaussian noise added to each measure of velocity dispersion. As  $\Delta$  increases, we expect the correlation to decrease. Such an experiment seeks to answer the following question: what type of additional random noise is needed to make the correlation of the population indices with velocity dispersion comparable to that of the trends with stellar mass? For reference, the latter are marked with a horizontal dashed line. In all cases we find that Gaussian noise at the level  $\Delta \sim 0.2$  dex can mimic the trends found. It is not uncommon to expect such an uncertainty in stellar mass estimates, although comparisons of independent methods suggest lower values, around  $\lesssim 0.1$  dex (see, e.g. Santini et al. 2015; Pacifici et al. 2023; Dogruel et al. 2023). These uncertainties are mainly produced by the methodology, regarding template fitting, mismatch of targeted populations, photometric error, fitting of the total luminosity, etc. The additional error we need in velocity dispersion is on the high side to bring the observed correlations with  $\sigma$  and  $M_s$  in line. Therefore we conclude that it may be possible to confirm  $\sigma$  as the major driver of population properties, but unknown uncertainties in the stellar mass may also make this parameter a major driver. In any case, note that while  $M_s$  and  $\sigma$  are found in very different ways, the trends are fully consistent with the ansatz that local variables determine, statistically, the stellar population properties in galaxies.

## 5 A NOTE ON THE LINK WITH THE EVOLUTIONARY STAGE

Once we determine the potential main driver of population properties over small scales, a question remains regarding the connection with the general evolutionary stage, as posed by the well-established bimodality in colour (Strateva et al. 2001b), line strengths (Angthopo et al. 2019) and star formation rate (Speagle et al. 2014). A clear separation is found with regards to star formation activity, or lack thereof, along with a intriguing transitioning phase, the Green Valley, that encode the details of the feedback mechanisms that quench galaxy growth (see, e.g. Schawinski et al. 2014; Salim 2014).

In this exercise, we focus on this evolutionary trend by adopting two classification schemes: one is the segregation into blue cloud (BC), green valley (GV) and red sequence (RS), as presented in Angthopo et al. (2019). In that paper, the selection is based on a bivariate plot formed by  $D_n(4000)$  and velocity dispersion, measured in the SDSS Legacy spectra, measured in single 3 arcsec diameter fibres. A second scheme is based on the traditional BPT (Baldwin et al. 1981) diagram. Using once more the analysis from the SDSS Legacy (single fibre) spectra, as presented in the data

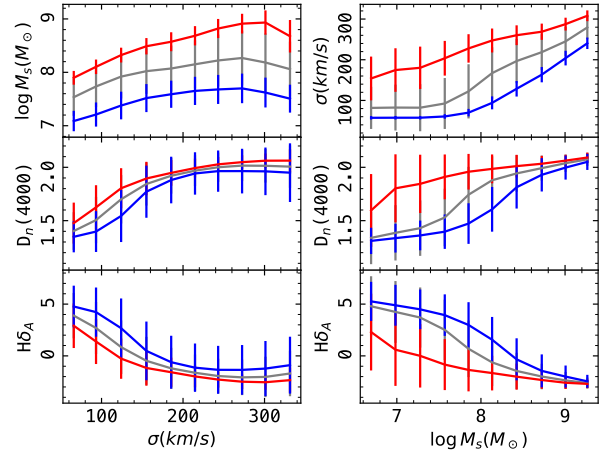


**Figure 6.** Evolution of the median of 4000Å break strength (middle) and  $H\delta_A$  (bottom) as a function of velocity dispersion (left) or stellar mass (right). The whole sample is shown in grey, along with the subsets at low (25 percentile, blue) and high (75 percentile, red) of the distribution within each bin in  $\sigma$  or  $\log M_s$ . The points are the median values, whereas the error bars represent the standard deviation in each bin. The top panels illustrate the sample selection strategy.

products of Brinchmann et al. (2004), we separate galaxies into quiescent (Q), star forming (SF) and AGN.

Fig. 8 shows the distribution of spaxel data with respect to  $\sigma$  for the three line strengths targeted in this paper. However, given that the classification method is based on the central spectra of galaxies, we restrict the sample to the outermost spaxels ( $R > 1.5R_e$ ). This allows us to explore the local properties of individual spaxels without introducing the obvious selection bias. The figure complements our previous results as the correlation remains in all cases. Unsurprisingly, the RS and Q data favours higher 4000Å break strengths and weaker Balmer absorption, along with higher  $[MgFe]'$ . The BC and SF sets mostly populate the regions expected by younger populations, whereas the GV and AGN live somewhere in between the two major cases of the bimodality. While this is an expected result, we should emphasize that these data correspond to spaxels outside of the regions where the selection was produced. Therefore, while we claim that sub-galaxy (around 2 kpc) scales drive the trends in the line strengths, the evolutionary stage (which is defined over galaxy scales) does indeed affect the distributions. In other words, the outside spaxels “know” they belong to a galaxy of a given evolutionary type.

Note also the interesting differences between both classification schemes (left vs right in Fig. 8). The RS sample does feature a substantial fraction of weak  $D_n(4000)$  data at low  $\sigma$ , in contrast with the Q sample. Similarly, the AGN vs GV comparison also suggests a fraction of AGN that would not be classified as GV. Note that the BPT selection relates to substantially shorter timescales (regarding the nebular emission of the diffuse gas), whereas the Angthopo et al. (2019) classification is based on the 4000Å break, therefore associated to the longer timescales of stellar evolution. The consistency confirms that the recent behaviour is statistically connected with those larger timescales.

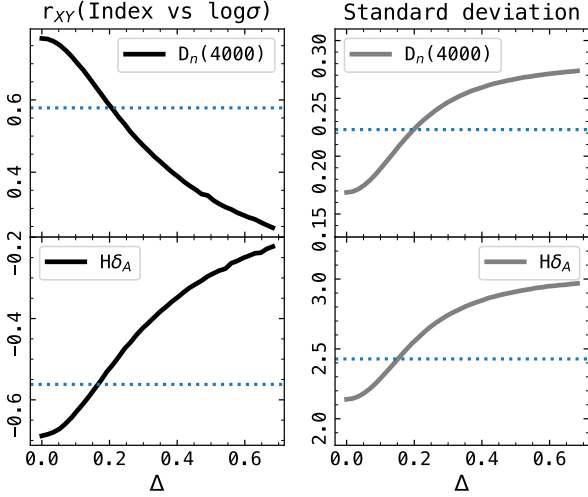


**Figure 7.** The correlation coefficient (left) and standard deviation of the residual (right) is shown as Gaussian noise is randomly added to the measurement of stellar velocity dispersion. Two line strengths are considered: 4000Å break (top) and  $H\delta_A$  (bottom). As the noise level ( $\Delta$ ) increases, the correlation (standard deviation) decreases (increases). For reference, the values obtained for the relations with respect to stellar mass are shown as blue horizontal dotted lines.

## 6 CONCLUSIONS

In this paper we make use of the SDSS-IV MaNGA IFU dataset (Bundy et al. 2015b) in a novel way: instead of exploring the data with galaxies as fundamental units, we adopt the ansatz that local properties – defined within each spaxel – determine the stellar population properties in a statistical way. Given that these properties relate to the star formation history, this claim goes beyond the standard framework, and provides an observational trend that any model of galaxy formation should be able to reproduce. Our sample involves 2,024 high quality IFU datacubes of galaxies at redshift  $0.05 < z < 0.1$  (median  $z_M=0.065$ ) from which we extract over one million spaxels, treated independently in this work, only to be related to quantities defined by the spaxels themselves. The analysis makes use of the Marvin data products (Cherinka et al. 2019).

From the set of local properties considered, we find that local stellar velocity dispersion is the one with the strongest correlation, although the intrinsically low systematics may be the reason that it fares better than stellar mass or stellar mass surface density. Galactocentric radial distance is readily ruled out as a fundamental driver, as it consistently shows lower correlation coefficients and higher scatter. In light of this, one should consider that radial gradients of galaxy properties are a consequence of radial variations in the local stellar velocity dispersion at different radii, a tracer of the gravitational potential. We also note that the dominant role of stellar velocity dispersion found in these data may parallel the strong trend between the central supermassive black hole mass and the velocity dispersion of the bulge (Ferrarese & Merritt 2000; Kormendy & Ho 2013). However, we should emphasize that the strong correlation found in our data extends to the spaxels in the outermost regions (see Fig. 8),

where the potential contamination from the bulge should be minimal, as illustrated in App. B.

Our results support and complement the suggestion of Sánchez et al. (2021) giving emphasis on sub-galaxy ( $\sim 2$  kpc) scales as dominant in the formation history of galaxies, with larger scales showing the equivalent of an integrated relation. Our analysis goes beyond short-timescale relations, such as those probed by emission lines. The trends with respect to stellar populations depend on substantially longer timescales and concern the star formation and chemical enrichment histories of galaxies. We also support the idea that galaxy-wide scales play some role, as suggested by Fig. 8, but the trends regarding smaller scales should be taken into account in any successful theory of galaxy formation.

Finally, it did not escape our attention that the correlations with line strength indicators are stronger than those with physical parameters such as age or metallicity, derived from population synthesis modelling. Given that the line strength measurements are observationally produced in an independent way to velocity dispersion, we propose that the model fitting process introduces a scatter that does not truly reflect the strong connection between star formation histories and local velocity dispersion.

## ACKNOWLEDGEMENTS

IF acknowledges support from the Spanish Research Agency of the Ministry of Science and Innovation (AEI-MICINN) under grant PID2019-104788GB-I00. MT acknowledges the support of CNPq (process #307675/2018-1). OL acknowledges STFC Consolidated Grant ST/R000476/1 and a Visiting Fellowship at All Souls College and at the Physics Department, Oxford. RRdC acknowledges the support from FAPESP through grant 2020/16243-3. Funding for SDSS-III has been provided by the Alfred P. Sloan Foundation, the Participating Institutions, the National Science Foundation, and the U.S. Department of Energy Office of Science. The SDSS-III web site is <http://www.sdss3.org/>.

## DATA AVAILABILITY

This work has been fully based on publicly available data: galaxy spectra were retrieved from the SDSS DR17 archive and stellar population synthesis models can be obtained from the respective authors. The excellent MaNGA/Marvin database can be accessed at [this link](https://www.manga.org/).

## REFERENCES

- Abdurro’uf et al., 2022, *ApJS*, 259, 35
- Anghthopo J., Ferreras I., Silk J., 2019, *MNRAS*, 488, L99
- Anghthopo J., Ferreras I., Silk J., 2020, *MNRAS*, 495, 2720
- Bacon R., et al., 2001, *MNRAS*, 326, 23
- Baldry I. K., Glazebrook K., Brinkmann J., Ivezić Ž., Lupton R. H., Nichol R. C., Szalay A. S., 2004, *ApJ*, 600, 681
- Baldwin J. A., Phillips M. M., Terlevich R., 1981, *PASP*, 93, 5
- Balogh M. L., Morris S. L., Yee H. K. C., Carlberg R. G., Ellingson E., 1999, *ApJ*, 527, 54
- Brinchmann J., Charlot S., White S. D. M., Tremonti C., Kauffmann G., Heckman T., Brinkmann J., 2004, *MNRAS*, 351, 1151

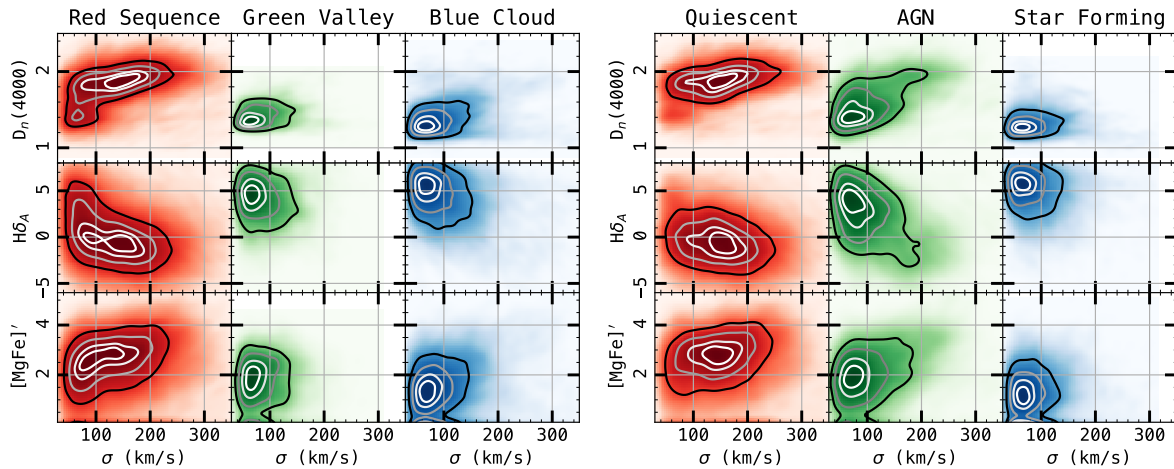


**Figure 8.** Line strength plot for galaxies segregated with respect to the classification of [Anghopo et al. \(2019\)](#) (Left) or regarding nebular activity via the standard BPT diagram (Right). The data points correspond to individual spaxels in the outermost regions of the chosen galaxies ( $>1.5R_e$ ,  $S/N > 5$ ).

Bryant J. J., et al., 2015, *MNRAS*, **447**, 2857  
 Bundy K., et al., 2015a, *ApJ*, **798**, 7  
 Bundy K., et al., 2015b, *ApJ*, **798**, 7  
 Cappellari M., et al., 2011a, *MNRAS*, **413**, 813  
 Cappellari M., et al., 2011b, *MNRAS*, **416**, 1680  
 Cherinka B., et al., 2019, *AJ*, **158**, 74  
 Dogruel M. B., Taylor E. N., Cluver M., D’Eugenio F., de Graaff A., Colless M., Sonnenfeld A., 2023, *ApJ*, **953**, 45  
 Etherington J., Thomas D., 2015, *MNRAS*, **451**, 660  
 Ferrarese L., Merritt D., 2000, *ApJ*, **539**, L9  
 Ferreras I., Charlot S., Silk J., 1999, *ApJ*, **521**, 81  
 Ferreras I., et al., 2019, *MNRAS*, **489**, 608  
 Ferreras I., Lahav O., Somerville R. S., Silk J., 2023, *RAS Techniques and Instruments*, **2**, 78  
 González Delgado R. M., et al., 2015, *A&A*, **581**, A103  
 Greene J. E., Janish R., Ma C.-P., McConnell N. J., Blakeslee J. P., Thomas J., Murphy J. D., 2015, *ApJ*, **807**, 11  
 Kennicutt Robert C. J., 1989, *ApJ*, **344**, 685  
 Kormendy J., Ho L. C., 2013, *ARA&A*, **51**, 511  
 Kuntschner H., et al., 2010, *MNRAS*, **408**, 97  
 La Barbera F., Ferreras I., de Carvalho R. R., Bruzual G., Charlot S., Pasquali A., Merlin E., 2012, *MNRAS*, **426**, 2300  
 La Barbera F., Ferreras I., Vazdekis A., de la Rosa I. G., de Carvalho R. R., Trevisan M., Falcón-Barroso J., Ricciardelli E., 2013, *MNRAS*, **433**, 3017  
 Naab T., Johansson P. H., Ostriker J. P., 2009, *ApJ*, **699**, L178  
 Oser L., Ostriker J. P., Naab T., Johansson P. H., Burkert A., 2010, *ApJ*, **725**, 2312  
 Pacifici C., et al., 2023, *ApJ*, **944**, 141  
 Parikh T., et al., 2018, *MNRAS*, **477**, 3954  
 Parikh T., Thomas D., Maraston C., Westfall K. B., Andrews B. H., Boardman N. F., Drory N., Oyarzun G., 2021, *MNRAS*, **502**, 5508  
 Pearl J., Mackenzie D., 2018, *The Book of Why: The New Science of Cause and Effect*. Basic Books, New York  
 Peng Y.-j., et al., 2010, *ApJ*, **721**, 193  
 Rogers B., Ferreras I., Pasquali A., Bernardi M., Lahav O., Kaviraj S., 2010, *MNRAS*, **405**, 329  
 Salim S., 2014, *Serbian Astronomical Journal*, **189**, 1  
 Sánchez S. F., et al., 2012, *A&A*, **538**, A8  
 Sánchez S. F., Walcher C. J., Lopez-Cobá C., Barrera-Ballesteros J. K., Mejía-Narváez A., Espinosa-Ponce C., Camps-Fariña A., 2021, *Rev. Mex. Astron. Astrofis.*, **57**, 3  
 Santini P., et al., 2015, *ApJ*, **801**, 97

Schawinski K., et al., 2014, *MNRAS*, **440**, 889  
 Schmidt M., 1959, *ApJ*, **129**, 243  
 Silk J., Mamon G. A., 2012, *Research in Astronomy and Astrophysics*, **12**, 917  
 Speagle J. S., Steinhardt C. L., Capak P. L., Silverman J. D., 2014, *ApJS*, **214**, 15  
 Strateva I., et al., 2001a, *AJ*, **122**, 1861  
 Strateva I., et al., 2001b, *AJ*, **122**, 1861  
 Thomas D., Maraston C., Bender R., 2003, *MNRAS*, **339**, 897  
 Wake D. A., et al., 2017, *AJ*, **154**, 86  
 Wang B., Peng Y., Cappellari M., 2024, *Nature Astronomy*,  
 Weinmann S. M., van den Bosch F. C., Yang X., Mo H. J., 2006, *MNRAS*, **366**, 2  
 Westfall K. B., et al., 2019, *AJ*, **158**, 231  
 Wilkinson D. M., Maraston C., Goddard D., Thomas D., Parikh T., 2017, *MNRAS*, **472**, 4297  
 Worthey G., Ottaviani D. L., 1997, *ApJS*, **111**, 377  
 Zibetti S., Gallazzi A. R., Hirschmann M., Consolandi G., Falcón-Barroso J., van de Ven G., Lyubenova M., 2020, *MNRAS*, **491**, 3562

## APPENDIX A: DISTRIBUTION OF LINE STRENGTHS FOR INDIVIDUAL GALAXIES

We show in Fig. A1 the distribution of line strengths measured in a few galaxies from the sample. From left to right they correspond to representative galaxies in the blue cloud, green valley and red sequence, respectively. Each diagram includes as coloured dots the 4000Å break strength with respect to stellar velocity dispersion, galactocentric distance (measured in fractions of the effective radius), and stellar mass surface density. Each panel also shows, as contours, the distribution of the total spaxel sample (i.e. the results of Fig. 2). For reference, a coloured stamp is included to the right of each set of panels, including in pink the footprint of the MaNGA IFU.

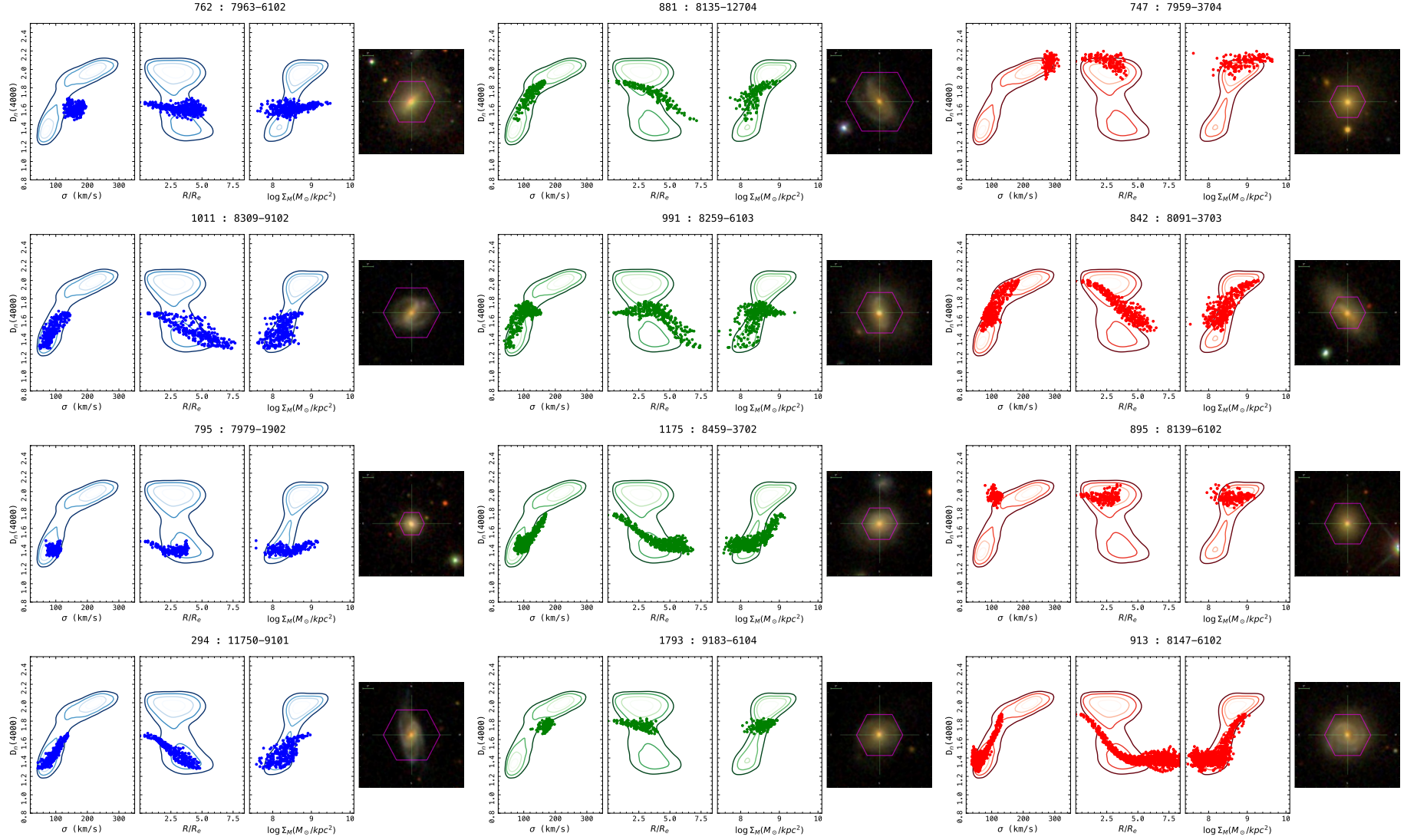


**Figure A1.** Distribution of spaxel measurements of  $D_n(4000)$  in a small selection of galaxies. A stamp of each galaxy is included for reference. The subset is colour coded regarding their identification – from [Anghopo et al. \(2019\)](#) – as blue cloud (left), green valley (middle) or red sequence (right).

## APPENDIX B: CORRELATION IN THE OUTERMOST SPAXELS

One might argue that most of the results in this sample could be mainly caused by the stellar populations in the central regions, i.e. dominated in most cases by the bulge component. In fact, the dominant role of velocity dispersion may be reminiscent of the well-known correlation between supermassive black hole mass and the velocity dispersion of the bulge (Ferrarese & Merritt 2000). In this appendix we show that the inherent trend cannot be simply ascribed to the bulge. Fig. B1 shows the equivalent of Fig. 2 for the subset of spaxels at galactocentric distance  $R \geq 5$  kpc (keeping the S/N threshold above 5). This subset comprises 460,203 spaxels, and the trends are consistent with the full sample – of course noting that, by construction, the range in galactocentric radii is restricted. In addition, we show in Tab. B1 the equivalent of Tab. 1 for these outermost spaxels. We conclude that neither the limited spatial resolution (PSF) nor the role of the bulge is significant in the trends found in this paper. Incidentally, note that the bimodality in the population indicators appears quite strongly at all of the outer radii, whereas the line strengths depend sensitively on the velocity dispersion.

This paper has been typeset from a  $\text{\TeX}/\text{\LaTeX}$  file prepared by the author.

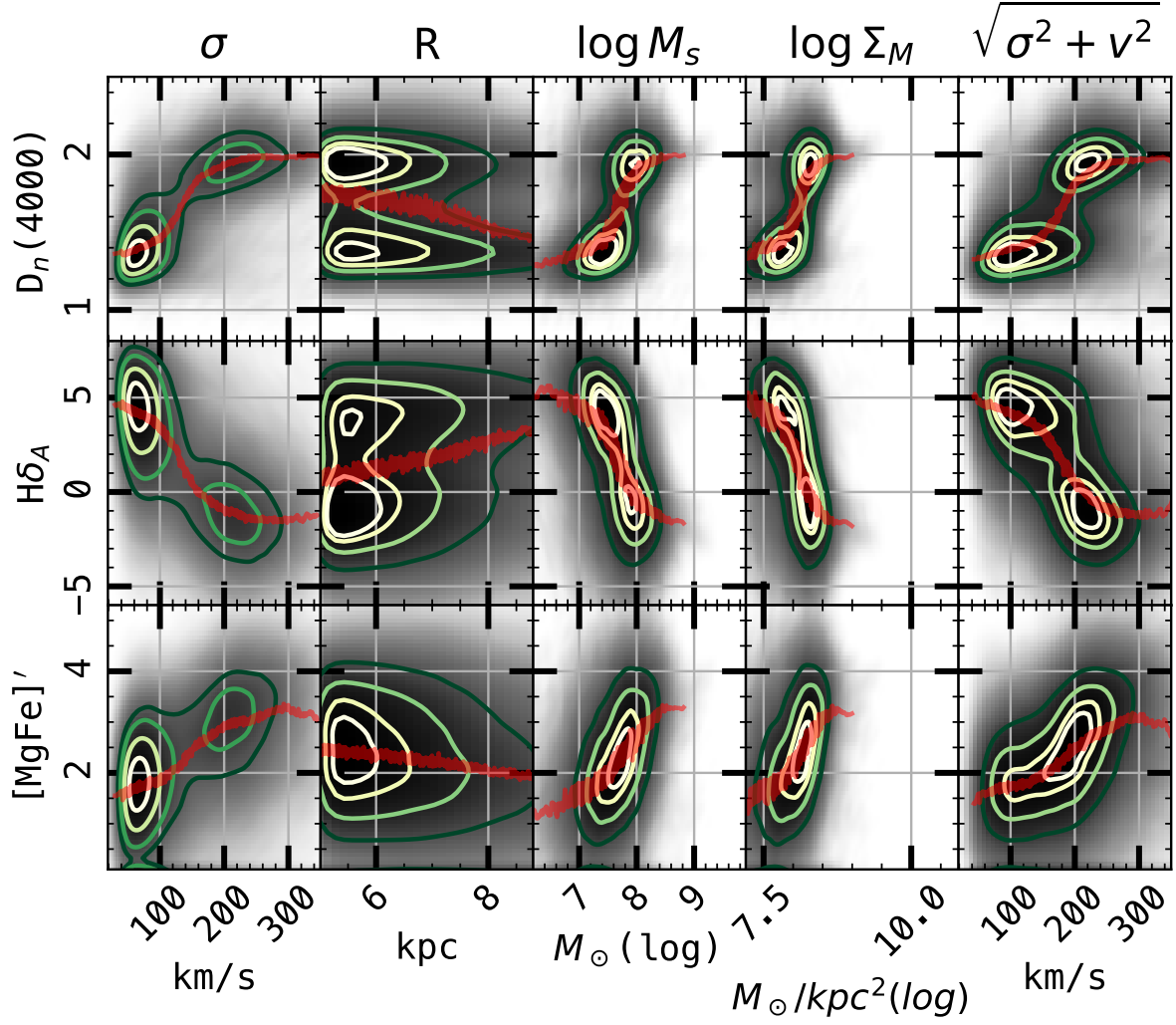


**Figure B1.** Equivalent of Fig. 2 for the subset of the outermost spaxels, located at galactocentric radial distance  $R \geq 5$  kpc.

**Table B1.** Correlation coefficients between stellar population line strengths and observables measured in an absolute way in spaxels with  $S/N \geq 5$  in the outermost spaxels ( $R \geq 5$  kpc, see fig B1)

Index	$\sigma$	$R$	$\log M_s$	$\log \Sigma_M$	$\sqrt{\sigma^2 + v^2}$
Correlation coefficient					
$D_n(4000)$	$+0.766 \pm 0.001$	$-0.193 \pm 0.001$	$+0.554 \pm 0.001$	$+0.534 \pm 0.001$	$+0.569 \pm 0.001$
$H\delta_A$	$-0.672 \pm 0.001$	$+0.193 \pm 0.001$	$-0.501 \pm 0.001$	$-0.510 \pm 0.001$	$-0.496 \pm 0.001$
$[MgFe]'$	$+0.513 \pm 0.001$	$-0.205 \pm 0.001$	$+0.425 \pm 0.001$	$+0.421 \pm 0.001$	$+0.334 \pm 0.002$
Standard deviation (and $1\sigma$ error)					
$D_n(4000)$	$0.175 \pm 0.031$	$0.289 \pm 0.013$	$0.240 \pm 0.030$	$0.242 \pm 0.032$	$0.224 \pm 0.043$
$H\delta_A$	$2.279 \pm 0.235$	$3.141 \pm 0.102$	$2.728 \pm 0.322$	$2.688 \pm 0.330$	$2.654 \pm 0.345$
$[MgFe]'$	$0.911 \pm 0.057$	$1.046 \pm 0.054$	$0.962 \pm 0.058$	$0.960 \pm 0.068$	$0.969 \pm 0.069$